Chalcogenide Letters Vol. 22, No. 12, December 2025, p. 1031-1045

Bismuth Silver Sulfide ($AgBiS_2$) Nanoparticle-Modified SPEs Enabling Concurrent Lead and Cadmium Analysis

Wenwen Zhang* and Changgui Lei

College of Food and Chemical Engineering, Henan Quality Institute, Pingdingshan, 467000, China
*Corresponding Author: Wenwen Zhang. Email: zuiqiangnuliumang@163.com

Received: 23 September 2025; Accepted: 8 December 2025

ABSTRACT: The development of quick, accurate, and field-deployable detection techniques is required due to the growing environmental pollution caused by heavy metals, especially lead (Pb) and cadmium (Cd). In this work, bismuth silver sulfide ($AgBiS_2$) nanoparticles are synthesized using a simple hydrothermal method aided by biomolecules, and they are used as a new modifier forPb(II) and Cd(II) simultaneous electrochemical detection using screen-printed electrodes (SPEs). After thorough material characterisation, pure, highly crystalline, quasi-spherical $AgBiS_2$ nanoparticles produced with an average diameter of around 20 nm. The $AgBiS_2$/SPE sensor demonstrated a threefold decrease in charge transfer resistance, indicating a considerable improvement in electrochemical performance. The sensor showed outstanding analytical performance under optimal SWASV, or square wave anodic stripping voltammetry conditions, with broad linear ranges and low 0.21 μg/L for Pb(II) and 0.15 μg/L for Cd(II) are the detection limits, both of which are far below WHO recommendations. Along with demonstrating great selectivity, good repeatability, and long-term stability,The sensor was successfully used to analyze real water samples, highlighting its promise as an affordable and reliable instrument for on-site environmental monitoring.

KEYWORDS: $AgBiS_2$; chalcogenide; nanoparticles; electrochemical sensor; heavy metals; lead; cadmium; screen-printed electrode

1 Introduction

One of the biggest environmental problems of the contemporary period is the widespread poisonous heavy metal poisoning of ecosystems. Because of their severe toxicity, lack of biodegradability, and propensity to bioaccumulate in living things, lead (Pb) and cadmium (Cd) are the most concerning of these pollutants [1]. Public health organizations categorize both elements as substances that are known to have serious negative health impacts, such as reproductive damage and birth deformities. Even at low concentrations, lead exposure, a well-established neurotoxic for which no safe threshold has been established, may cause irreparable brain damage, learning impairments, and a decrease in IQ [2]. Lead exposure is especially dangerous for children. Cadmium is a known human carcinogen that may cause serious harm to the kidneys, liver, and bones when exposed over an extended period of time [3]. Anthropogenic activities including mining, smelting, burning fossil fuels, and using certain fertilizers and pesticides are the main ways that these metals enter the environment and cause extensive pollution of the soil, water, and food chain. The development of sensitive, accessible, and dependable techniques for monitoring Pb and Cd levels is vital for environmental and public health protection due to their persistence and significant health effects.

Traditional analytical methods for detecting trace Detecting heavy metals using techniques like Inductively Coupled Plasma-Mass Spectrometry (ICP-MS) and Atomic Absorption Spectroscopy (AAS) is considered as the gold standard because they providevery low detection limits, often in the region of parts per trillion (ppt) [4]. However, there are several barriers that make it difficult to use these techniques in practice for regular and extensive environmental screening. High initial and ongoing expenses, intricate maintenance needs, and the demand for highly skilled workers to operate them are characteristics of these devices [5]. They are also solely confined to laboratories because to their size and the strict infrastructure needs of the lab, including the significant consumption of pure argon gas. For on-site, real-time monitoring applications, they are inappropriate. due to their intrinsic lack of mobility, which requires sample collection, transit,

https://doi.org/10.15251/CL.2025.2212.1031

and storage. This not only causes delays in the findings, but also raises the possibility of sample contamination and analytical mistake.

A strong and alluring substitute for conventional spectroscopic techniques, electrochemical sensing devices successfully meet the need for field-deployable analysis. These sensors are perfect for *in-situ* monitoring of environmental contaminants because of their many benefits, which include cheap cost, mobility, quick reaction times, great sensitivity and user-friendliness [6]. By using nanomaterials to modify the electrode surface, which offer a high surface-area-to-volume ratio and special catalytic properties that promote more effective analyte interaction and signal transduction, the performance of electrochemical sensors can be significantly improved [7]. SWASV, or square wave anodic stripping voltage, is an electrochemical methods that works well for trace metal analysis. In order to detect at extremely low concentrations, this technique combines an efficient pre-concentration stage in which target metal ions are reductively deposited onto the working electrode surface. This is followed by a quick stripping process that produces a very sensitive analytical signal [8].

An electrochemical sensor's success depends critically on the choice of modifier material. Ternary bismuth silver sulfide ($AgBiS_2$) nanoparticles are presented in this study as a unique and very efficient sensing material. Being made up of inexpensive, non-toxic, and earth-abundant elements, $AgBiS_2$, a member of the I-V-VI_2 chalcogenide family, is positioned as an eco-friendly or "green" substitute for widely used but dangerous semiconductor materials like lead- or cadmium-based quantum dots [9]. The synergistic electrochemical characteristics of its component parts serve as the foundation for the reasoning for its selection. Because bismuth can form fusible alloys with both lead and cadmium, which facilitates their deposition and improves the subsequent stripping signal, resulting in improved sensitivity and well-resolved peaks, bismuth-based electrodes are well known for their effectiveness in heavy metal detection [10]. At the same time, silver is anticipated to provide the nanocomposite strong electrical conductivity, guaranteeing quick electron transfer kinetics at the electrode-solution interface. $AgBiS_2$ nanoparticles may be a remarkable platform because of this special combination of properties, for the simultaneous and very sensitive detection of Pb(II) and Cd(II).

Therefore, the purpose of this study is to use a straightforward hydrothermal process supported by biomolecules to manufacture and thoroughly analyze unique $AgBiS_2$ nanoparticles. A disposable, inexpensive modified screen-printed electrode ($AgBiS_2$/SPE) is then created using these nanoparticles. With the ultimate goal of creating a useful instrument for on-site environmental analysis, the main objective is to methodically assess and validate the analytical performance of this innovative sensor for the sensitive, selective, and concurrent electrochemical determination of Pb(II) and Cd(II) ions in aqueous solutions.

2 Materials and Methods

2.1 Chemicals and Reagents

The materials supplied by Sigma-Aldrich included silver nitrate ($AgNO_3$, ≥99.0%), bismuth(III) nitrate pentahydrate ($Bi(NO_3)_3·5H_2O$, ≥98.0%), L-cysteine (≥98.5%), lead(II) nitrate ($Pb(NO_3)_2$, ≥99.0%), and cadmium(II) nitrate tetrahydrate ($Cd(NO_3)_2·4H_2O$, ≥98.0%). Hydrochloric acid (HCl, 37%), sodium acetate (anhydrous, ≥99.0%), potassium chloride (KCl, ≥99.0%), potassium ferricyanide ($K_3[Fe(CN)_6]$, ≥99.0%), and potassium ferrocyanide trihydrate ($K_4[Fe(CN)_6]·3H_2O$, ≥98.5%) were all supplied by Merck. Additionally, Sigma-Aldrich supplied us with N,N-Dimethylformamide (DMF, 99.8%). Analytical-grade chemicals were all utilized just as supplied, requiring no further purification. Stock solutions of Pb(II) and Cd(II) at 1000 mg/L were made by dissolving the corresponding nitrate salts in ultrapure deionized water. Every day, the stock solutions were serially diluted to create working solutions with decreasing concentrations. The supporting electrolyte,By mixing the appropriate quantities of sodium acetate and acetic acid solutions and adjusting the pH as needed, 0.1 M acetate buffer solution (ABS) was created.

2.2 Synthesis of $AgBiS_2$ Nanoparticles

A simple hydrothermal process aided by biomolecules was used to create the $AgBiS_2$ nanoparticles (NPs) [11]. 1.0 mmol of AgNO3 (0.169 g) and 1.0 mmol of $Bi(NO_3)_3·5H_2O$ were dissolved in 40 mL of deionized water using a conventional procedure. (0.485 g) in a glass beaker while being stirred magnetically. 3.0 mmol of L-cysteine (0.363 g) was added to this clear solution. Through the thermal breakdown of its thiol group, L-cysteine acts as a sulfide source. It also complexes with metal cations to assist regulate the nucleation and development of the nanoparticles. For half an hour, the liquid was rapidly agitated until a uniform suspension was successful. Following that, this suspension was placed in a 50 mL Teflon-lined stainless-steel autoclave, sealed, and baked for 24 h at 200°C. The autoclave was allowed to naturally cool to room temperature after the reaction. Centrifugation was used for 10 min at 8000 rpm to collect the resultant black precipitate. The product underwent centrifugation and redispersion procedures after beingwashed twice with deionized water and three times with 100% ethanol to get rid of any unreacted precursors and soluble byproducts. The purified $AgBiS_2$ NPs were then dried in a vacuum oven for 12 h at 60°C.

2.3 Fabrication of the Modified Electrode ($AgBiS_2$/SPE)

Using a straightforward drop-casting technique, the $AgBiS_2$-modified screen-printed electrode ($AgBiS_2$/SPE) was created [12]. The first step included mixing 5.0 mg of the as-synthesised $AgBiS_2$ NPs with 5.0 mL of DMF to create a stable nanoparticle dispersion. After 30 min of ultrasonication, the mixture formed a uniform black dispersion with a 1.0 mg/mL concentration. Commercial screen-printed carbon electrodes contained a silver pseudo-reference electrode, a carbon counter electrode, and a carbon working electrode (4 mm diameter). (SPEs, DropSens DRP-110) that were used as the substrate. Before being altered, the working electrode's surface was cleaned with ethanol and deionized water and let to dry. The active region was then thoroughly covered by gently pipetting a 5 µL aliquot of the $AgBiS_2$ NP dispersion over the carbon working electrode's surface [13]. A homogenous and stable layer of $AgBiS_2$ nanoparticles formed on the electrode surface as a consequence of the electrode being put in an oven set at 50°C for 15 min. This process allowed the DMF solvent to evaporate gradually. The prepared $AgBiS_2$/SPEs were kept at room temperature and in a dry, dark place when not in use. SPEs that had not been altered (bare) served as a control in every experiment.

2.4 Electrochemical Measurements

At room temperature, all electrochemical measurements were conducted using three electrodes in a 25 mL electrochemical cell. An Ag/AgCl electrode (3 M KCl) served as the reference electrode, bare SPE or $AgBiS_2$/SPE served as the working electrode, and platinum wire served as the counter electrode. The fundamental electrochemical properties of the electrodes were examined using Electrochemical Impedance Spectroscopy (EIS) and Cyclic Voltammetry (CV). These investigations were conducted using a 5.0 mM

[Fe(CN)6]3−/4− solution with 0.1 M KCl as the supporting electrolyte. CV scans were acquired between −0.2 V and +0.6 V at a scan rate of 50 mV/s. To test EIS at the formal potential of the redox probe, a sinusoidal AC voltage with an amplitude of 10 mV was supplied between 100 kHz and 0.1 Hz [14].

The simultaneous detection of Pb(II) and Cd(II) in 0.1 M acetate buffer (pH 5.0) was accomplished using SWASV. The SWASV method consisted of two main stages: stripping and deposition. The solution was continuously swirled for 180 s while a voltage of −1.2 V was applied to the working electrode to encourage the deposition of target metals onto the electrode surface. After the deposition, the stirring was halted, and the system was given ten seconds to settle down and equilibrate.

3 Results and Discussion

3.1 Physicochemical Characterization of $AgBiS_2$ Nanoparticles

Utilizing X-ray diffraction, the crystalline structure was investigated. and phase purity of the hydrothermally produced $AgBiS_2$ nanoparticles. Several distinct diffraction peaks with 2θ values of 27.5°, 31.8°, 45.5°, 53.9°, and 56.4° are seen in the XRD pattern, which is shown in Fig. 1. The cubic rock-salt (Schapbachite) phase of $AgBiS_2$ contains the following crystal planes: (111), (200), (220), (311), and (222) (JCPDS Card No. 17-0456). [15] correspond to these peaks, respectively. The high phase purity of the synthesized product is confirmed by the lack of any noticeable peaks that would indicate binary sulfides (such as Ag_2S or Bi_2S_3) or other contaminants. A high degree of crystallinity is indicated by the diffraction peaks' sharpness and intensity. The average crystallite size (D) was calculated from the full width at half maximum (FWHM) of the most intense (200) diffraction peak using the Debye-Scherrer equation, $D = K\lambda/(\beta\cos\theta)$. This equation, The symbols K, λ, β, and θ represent the Scherrer constant (0.9), X-ray wavelength (0.15406 nm), FWHM (in radians), and Bragg angle, respectively. The material's nanocrystalline structure was confirmed by the computed average crystallite size of around 18 nm [16].

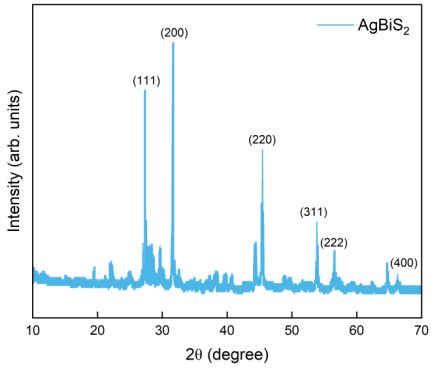

Figure 1: High crystallinity and phase purity are confirmed by the XRD pattern of hydrothermally produced $AgBiS_2$ nanoparticles, which displays distinctive diffraction peaks indexed to the cubic rock-salt phase (JCPDS No. 17-0456).

Scanning and transmission electron microscopy were used to further analyze the $AgBiS_2$ NPs' shape and microstructure. The result is composed of quasi-spherical nanoparticles that tend to form bigger agglomerates, as is typical for nanoparticles synthesized using hydrothermal techniques without strong capping agents, according to FESEM images taken at various magnifications (Fig. 2a,b). TEM examination was done to get a closer look at each individual nanoparticle. The nanoparticles' approximately spherical form and relative monodispersity are confirmed by the TEM images (Fig. 3a,b). The average diameter of the particle size distribution histogram, which was created by measuring more than 100 particles from the TEM pictures, is around 20 nm, which is quite consistent with the crystallite size as derived from the XRD data. The crystalline quality of a single nanoparticle may be inferred from the high-resolution TEM

(HRTEM) picture (Fig. 3c). With a measured interplanar the (200) plane of the cubic $AgBiS_2$ crystal structure, which is separated by 0.285 nm, distinct and well-ordered lattice fringes are evident [17]. The (111), (200), (220), and (311) planes of cubic $AgBiS_2$. The selected area electron diffraction (SAED) pattern (Fig. 3d) displays diffraction rings. The unique ring pattern attests to the synthetic material's polycrystalline nature [18].

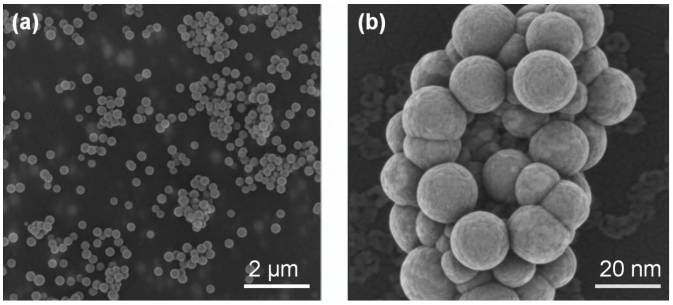

Figure 2: $AgBiS_2$ nanoparticles shown in FESEM pictures: Semi-spherical shape is shown in (**a**) the low-magnification view; aggregation of nanoparticles is seen in (**b**) the higher-magnification picture.

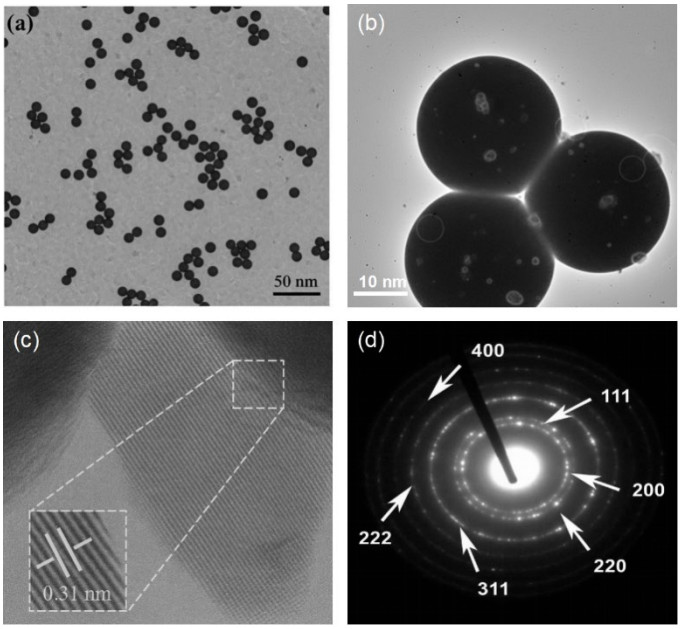

Figure 3: Identification of $AgBiS_2$ nanoparticles by TEM: (**c**) HRTEM picture with lattice fringes (d-spacing 0.31 nm, (200) plane); (**d**) SAED pattern verifying polycrystalline nature; (**a**,**b**) monodisperse spherical particles.

Using X-ray photoelectron spectroscopy, the chemical valence states and surface elemental composition of the generated $AgBiS_2$ NPs were investigated. Ag's presence, Bi, and S, as well as adventitious carbon (C 1s) and oxygen (O 1s), which are often seen as a result of surface adsorption from the surrounding environment, is evident in the XPS survey spectrum (Fig. 4a). To ascertain the oxidation states, high-resolution XPS spectra were captured for the core levels of Ag 3d, Bi 4f, and S 2p. The Ag 3d spectra deconvolutes into two separate peaks with 368.1 eV and 374.1 eV binding energies, which represent the Ag 3d5/2 and Ag 3d3/2 spin-orbit doublets, respectively, as shown in Fig. 4b. These 6.0 eV separates the peaks, which is indicative of the Ag^+ oxidation state. Two peaks located at 158.5 eV and 163.8 eV are ascribed to the Bi 4f7/2 and Bi 4f5/2 core levels in the high-resolution Bi 4f spectrum (Fig. 4c). Bismuth is confirmed to be present in the Bi^{3+} oxidation state by thedivide between spin and orbit of 5.3 eV [19]. With binding energies of 161.3 eV and 162.5 eV, respectively, the doublet in the S 2p spectrum (Fig. 4d) represents S

2p3/2 and S 2p1/2. The sulphide anion (S^{2-}) was found in metal sulfide compounds exhibits these values. The ternary complex $AgBiS_2$ is formed with the elements in their anticipated Ag^+, Bi^{3+}, and S^{2-} valence states, and the XPS findings are completely consistent with this.

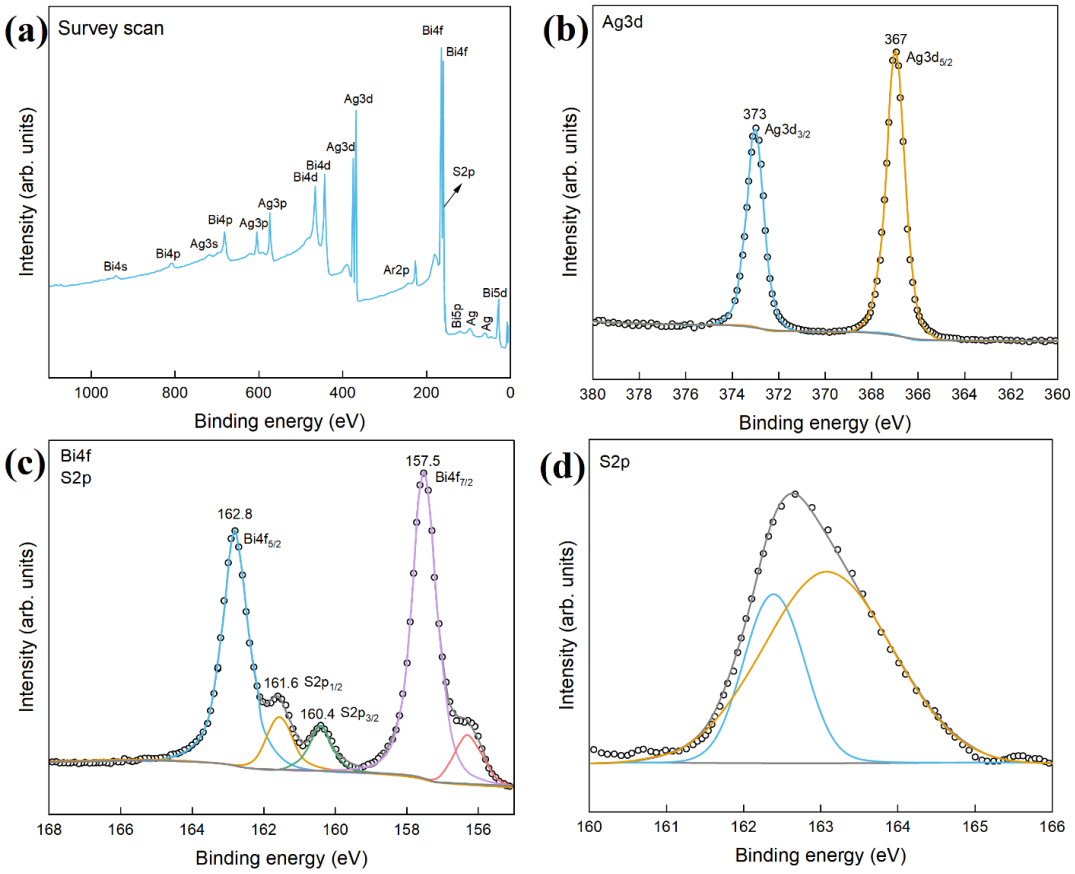

Figure 4: Analysis of $AgBiS_2$ nanoparticles using XPS: (**a**) survey spectrum displaying Ag, Bi, and S signals. (**b**) Ag 3d spectrum demonstrating Ag^+ state; (**c**) Bi 4f spectrum verifying Bi^{3+} state; (**d**) S 2p spectrum attributed to S^{2-} species;

The function of L-cysteine as the sulfur source in the hydrothermal synthesis was verified by FTIR spectroscopy. The FTIR spectra of the as-synthesised $AgBiS_2$ NPs and pure L-cysteine are shown in Fig. 5. L-cysteine's spectra shows a number of distinctive absorption bands, including a noticeable peak at around 2550 cm^{-1} that is associated with the thiol (-SH) group's stretching vibration. This -SH peak is totally missing from the $AgBiS_2$ NPs spectra. This discovery clearly suggests that during the hydrothermal process, the thiol group of L-cysteine was broken down, releasing sulfide ions that then interacted with the Ag^+ and Bi^{3+} cations to generate the $AgBiS_2$ product [20]. The $AgBiS_2$ spectrum also shows a considerable reduction or absence of other typical peaks of L-cysteine, such as those associated with the amine ($-NH_2$) and carboxyl (-COOH) groups. This suggests that the majority of the organic precursor was either degraded or successfully eliminated during the washing process. The C-H stretching from trace residual organic matter is responsible for the remaining weak bands, which are located between 2920 cm^{-1} and 2850 cm^{-1}.

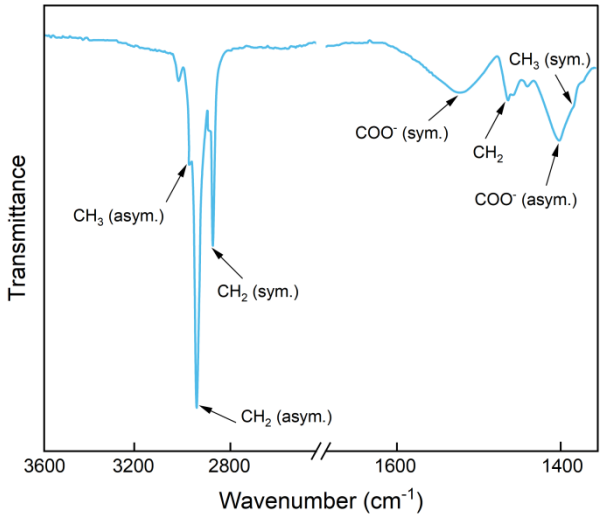

Figure 5: FTIR spectra of L-cysteine and $AgBiS_2$ NPs.

UV-vis absorption spectroscopy was used to examine the $AgBiS_2$ NPs' optical characteristics. Fig. 6a displays the wide and strong absorption spectra of the nanoparticles dispersed in toluene, which extends from the ultraviolet through the whole visible spectrum and into the near-infrared region [18]. $AgBiS_2$ is a potential material for a variety of optoelectronic applications, including photovoltaics and photodetectors, because to its wide absorption [21]. With the use of The Tauc relation for semiconductors with a straight band gap. The visible band gap (Eg) of the substance is $(\alpha h\nu)^2 = A(h\nu - Eg)$, where α is the absorption coefficient, hν is the photon energy, and A is a constant. semiconductor nanoparticles was calculated from the absorption data. The direct optical band gap was calculated to be about 1.35 eV when $(\alpha h\nu)^2$ is plotted versus hν and the linear portion of the curve to the energy axis (Fig. 6b). This number, which is referred to as a "blue shift," is far more than the stated band gap for bulk $AgBiS_2$ (around 0.9 eV). The effective production of nanoparticles is further shown by this shift, which is a direct result of the quantum confinement effect, which happens when the particle size is equal to or less than the exciton Bohr radius.

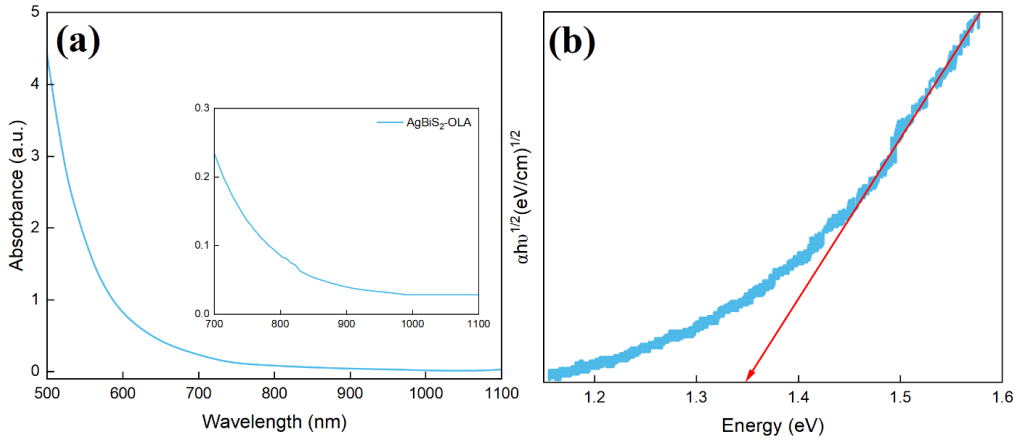

Figure 6: The $AgBiS_2$ nanoparticles' UV–vis absorption spectrum (**a**) demonstrates wide absorption over UV–vis–NIR regions; (**b**) a tauc plot is utilized to estimate a direct band gap of around 1.35 eV.

The specific surface area of the $AgBiS_2$ NPs was measured using nitrogen adsorption-desorption tests at 77 K. porosity. According to the IUPAC classification, the resultant isotherm, shown in Fig. 7, is a Type

III isotherm. Non-porous or macroporous materials with weak adsorbate-adsorbent interactions are characterized by this kind of isotherm [22]. Using The specific surface area was found to be 25.2 m^2/g using the Brunauer-Emmett-Teller (BET) method [23]. The only one that tiny particle size directly contributes to the comparatively large specific surface area, which is very beneficial for electrochemical sensing applications. Enhancing the sensor's sensitivity and overall functionality should be accomplished by a bigger region as it provides more easily accessible active spots for the electrochemical deposition process and stripping of the target heavy metal ions.

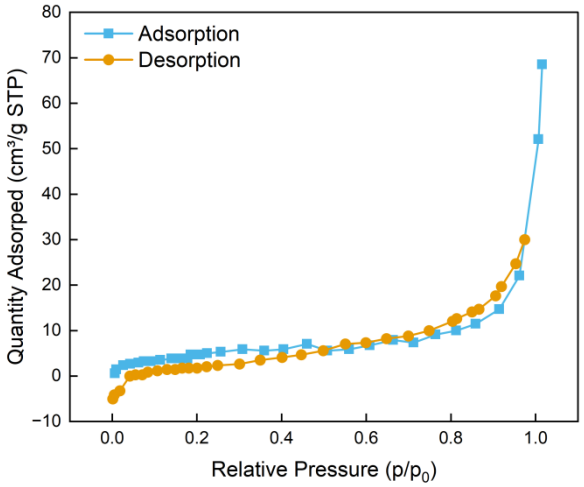

Figure 7: $AgBiS_2$ nanoparticles' nitrogen adsorption–desorption isotherm, which shows a type III isotherm.

3.2 Electrochemical Characterization of the Modified Electrode

With the $[Fe(CN)_6]^{3-/4-}$ redox pair, CV and EIS were used to examine the electrochemical characteristics of the naked SPE and the $AgBiS_2$/SPE. The cyclic voltammograms obtained at both electrodes are shown in Fig. 8a. With a wide peak-to-peak separation (ΔEp) of 195 mV and two broad redox peaks, the bare SPE shows slow electron transport kinetics. $AgBiS_2$/SPE, on the other hand, shows considerably improved electrochemical performance. The ΔEp drops to 115 mV, and the anodic and cathodic peak currents are much greater. While the reduced ΔEp is a definite sign of easier electron transport at the electrode-solution interface, the rise in peak current indicates a greater electroactive surface area and/or quicker kinetics [24].

To further investigate the electrodes' interfacial characteristics, EIS was used. A useful tool for examining charge transfer processes is the Nyquist plot, which shows the connection from the hypothetical (−Z″) to the actual (Z′) components of this impedance. The Nyquist plot for both electrodes, as shown in Fig. 8b, has a linear portionThe charge transfer resistance (Rct) is shown as a semicircle at high frequencies, while the diffusion process is linked to low frequencies. A direct indicator of Rct is the semicircle's diameter. A sizable semicircle with an estimated Rct of around 1480 Ω is seen in the bare SPE. The semicircle diameter is much lower for the $AgBiS_2$/SPE, resulting in a Rct value of only 750 Ω. The $AgBiS_2$ nanoparticle modification produces a highly conductive surface that greatly speeds up how quickly electrons move between the electrode and the redox probe in solution, as shown by the threefold reduction in charge transfer resistance [25]. For voltammetric sensing applications to achieve high sensitivity, this improved conductivity and kinetic facility are essential. A distinct structure-function relationship is established by the combined findings of the thorough physicochemical and electrochemical characterization: the synthesis process yields pure, highly crystalline nanoparticles with a large surface area and exceptional Conductivity of electricity, which in turn produce an excellent electrochemical interface for sensing applications.

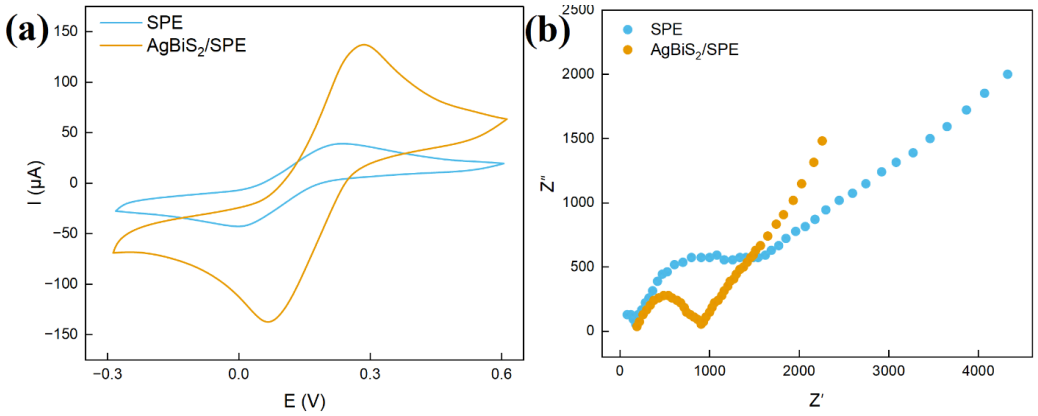

Figure 8: Electrochemical analysis of $AgBiS_2$/SPE and bare SPE: (**a**) $[Fe(CN)_6]^{3-/4-}$ CV curves in; (**b**) Nyquist plots from EIS demonstrating decreased charge transfer resistance upon modification.

3.3 Optimization of SWASV Parameters

A mixture with fifty micro grams per liter of each metal ion was used to systematically tune a number of important experimental parameters of the SWASV technique to get the greatest possible analytical performance for the simultaneous detection between the metals Cd(II) and Pb(II). Because it influences both the condition ofthe metal ion speciation in solution and the electrode surface, and pH of the supporting electrolyte is a crucial component. Using 0.1 M acetate buffer, the impact of pH was examined throughout the range of 3.5 to 6.0. The stripping peak currents for Pb(II) and Cd(II) both rose when the pH was elevated from 3.5 to 5.0, peaking at pH 5.0, as shown in Fig. 9a. Lower pH levels cause the metal cations to compete with the higher concentration of protons (H+) for active sites on the electrode surface, which prevents them from depositing and results in reduced signals [6]. On the other hand, peak currents started to drop at pH values higher than 5.0. This is because metal hydroxide complexes ($Pb(OH)_2$ and $Cd(OH)_2$) formed, which decreased the concentration of free, electroactive ions available for deposition. Therefore, the ideal pH for all next studies was determined to be 5.0.

The pre-concentration step's efficiency is directly impacted by the deposition potential. By changing the potential from −0.9 V to −1.4 V for a given deposition duration of 180 s, its impact was investigated. As the deposition potential becomes more negative, the stripping peak currents for both metals rise, plateauing at around −1.2 V, according to the findings, which are shown in Fig. 9b. The analytical signal did not significantly rise when potentials more negative than −1.2 V were applied; however, the background current did increase, most likely as a consequence of the hydrogen evolution process starting on the electrode surface [26]. In order to guarantee effective metal deposition while preserving a minimal background signal, −1.2 V was determined to be the ideal deposition potential [27].

The quantity of analyte deposited on the electrode surface is determined by the deposition period, which is also directly correlated with the measurement's sensitivity. At the ideal deposition potential of −1.2 V, and the effects of deposition time were investigated between 30 and 300 s. The peak currents The growth of both Pb(II) as Cd(II) levels is linear in relation to deposition time up to 240 s, as shown in Fig. 9c. This linear connection shows that, within this range, the quantity of metal deposited is proportionate to the accumulation time. The rate of growth slows down for durations more than 240 s, indicating that the electrode surface is getting close to saturation [28]. For the quantitative analysis, 180 s of formation time were employed to order to balance attaining high sensitivity with keeping a realistic analysis time.

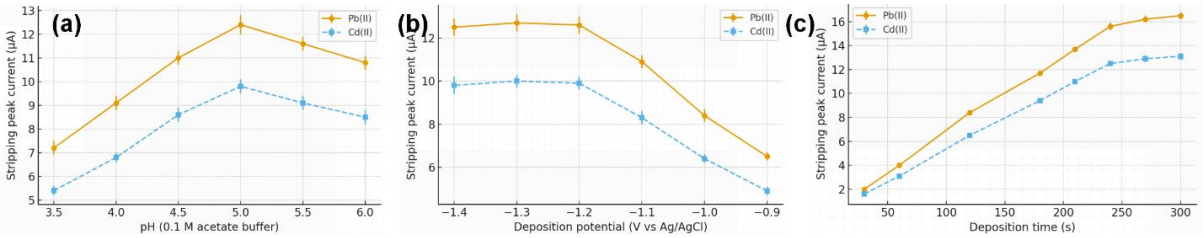

Figure 9: Optimization of SWASV parameters for Pb(II) and Cd(II) detection at $AgBiS_2$/SPE: (**a**) effect of pH (3.5–6.0); (**b**) effect of deposition potential (–0.9 to –1.4 V); (**c**) effect of deposition time (30–300 s).

3.4 Analytical Performance of the $AgBiS_2$/SPE Sensor

The analytical capabilities offered by $AgBiS_2$/SPE for Pb(II) and Cd(II) simultaneous detection was assessed underdetails ideal experimental circumstances (pH, 5.0, 180-s formation duration, −1.2 V formation prospective). details SWASV responses for increasing concentrations of both metal ions are shown in Fig. 10a. At potentials ofThe oxide formation of both lead and zinc is represented by values of about −0.85 V & −0.60 V, respectively, two separate and well-defined anodic stripping peaks are seen. The sensor's appropriateness for quantitative analysis is shown by the peak currents for both metals rising systematically with increasing concentration.

Calibration curves were created using the connection between the analyte concentration and the stripping peak current, as shown in Fig. 10b. Excellent linearity is shown by the sensor throughout a broad concentration range. With a linear regression equation of ICd (µA) = 0.85 × C_{Cd} (µg/L) + 0.5 and a correlation coefficient (R^2) of 0.998, the linear range ranges from 0.5 µg/L up 100 g per liter for Cd(II). 0.5 µg/L is the linear range of Pb(II). to 120 µg/L, an R^2 of 0.999, and a regression equation of I_{Pb} (µA) = 0.60 × C_{Pb} (µg/L) + 0.3. Within these ranges, a strong linear connection and excellent accuracy are shown by the high correlation coefficients. The formula LOD = 3σ/S was used in order to establish the detection limit, where σ is the calibration curve's standard deviation and S is the sensitivity, or slope. blank signal (n = 10). Regarding Pb(II) and Cd(II), the determined LODs were 0.21 µg/L and 0.15 µg/L, in that order. The one that World Health Organization's (WHO) maximum allowable values. Cd and Pb levels in drinking water are 3 µg/L and 10 µg/L, respectively, are far higher than these detection limits. This great sensitivity highlights the $AgBiS_2$/SPE's potential for useful environmental monitoring.

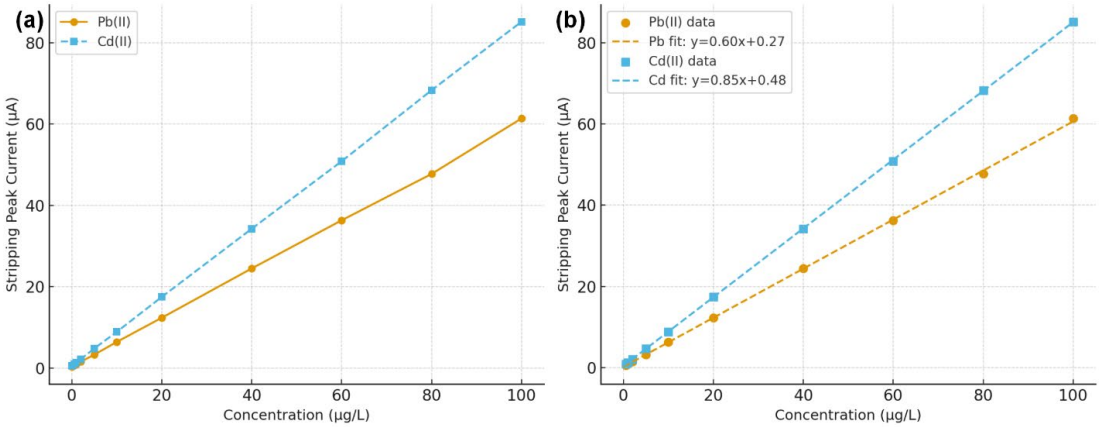

Figure 10: (**a**) SWASV responses of $AgBiS_2$/SPE for simultaneous detection of Pb(II) and Cd(II) at increasing concentrations and (**b**) corresponding calibration curves showing excellent linearity for both metals.

3.5 Validation of the Sensor and Mechanistic Discussion

An electrochemical sensor's selectivity is a crucial factor in real-world samples, which often include a complicated matrix of coexisting ions. By measuring the SWASV response to Pb(II) and Cd(II) solutions

with 20 µg/L each in the surroundings of a 100-fold excess of various potentially interfering ions commonly found in natural waters, such as Na^{+}, K^{+}, Mg^{2+}, Ca^{2+}, Zn^{2+}, and Cu^{2+}, the anti-interference capability of the $AgBiS_2$/SPE was evaluated. The bar chart in Table 1 provides a summary of the findings. The presence had little impact on the Pb(II) and Cd(II) stripping signals.common alkali and alkaline earth metals, with signal variations of less than 3%. The signal fluctuation was less than 5% even for otherIn particular, Zn^{2+} and Cu^{2+} are heavy metal ions that are known to possibly interfere via the creation of intermetallic compounds. This exceptional selectivity is a natural property of the material design and is not a result of chance. Bismuth's high thermodynamic inclination to create fusible alloys, particularly with lead and cadmium, is the source of the performance. The deposition and nucleation of Pb and Cd on the bismuth sites inside the $AgBiS_2$ nanoparticle surface are made possible by this strong chemical affinity, which efficiently outcompetes other ions. This inherent selectivity makes the sensor more useful for on-site analysis by minimizing matrix effects and lowering the requirement for masking chemicals, which streamlines the analytical process.

Table 1: Effect of interfering ions on the SWASV response of 20 µg/L Pb(II) and Cd(II) at the $AgBiS_2$/SPE.

Interfering Ion	Concentration Ratio (Interferent:Analyte)	Signal Change for Cd(II) (%)	Signal Change for Pb(II) (%)
Na^+	100	−1.8	−1.5
K^+	100	−2.1	−1.9
Mg^{2+}	100	−2.5	−2.2
Ca^{2+}	100	−2.3	−2.6
Zn^{2+}	100	−4.1	−3.8
Cu^{2+}	100	−4.8	−4.5

To determine the sensor's dependability, its stability and repeatability were also examined. Five separate $AgBiS_2$/SPEs were prepared, and their SWASV response to a mixture with 50 µg/L of Cd(II) and Pb(II) was measured in order to ascertain the manufacturing reproducibility. The relative deviations from average (RSDs) for Pb(II) and Cd(II) are 4.1% and 3.8%, respectively. were obtained from the measurements, as shown in Fig. 11a, demonstrating exceptional consistency and dependability in the electrode construction procedure. A single $AgBiS_2$/SPE was stored at 4°C and measurements were taken at regular intervals for four weeks in order to examine its long-term stability. After 28 days, the electrode maintained 96.5% of its original response regarding the amount of Cd(II) and 95.6 percent for Pb(II), as per the data displayed in Fig. 11b. This remarkable stability shows how durable the $AgBiS_2$ nanoparticle layer is on the SPE surface and how well-suited it is for long-term storage or frequent usage.

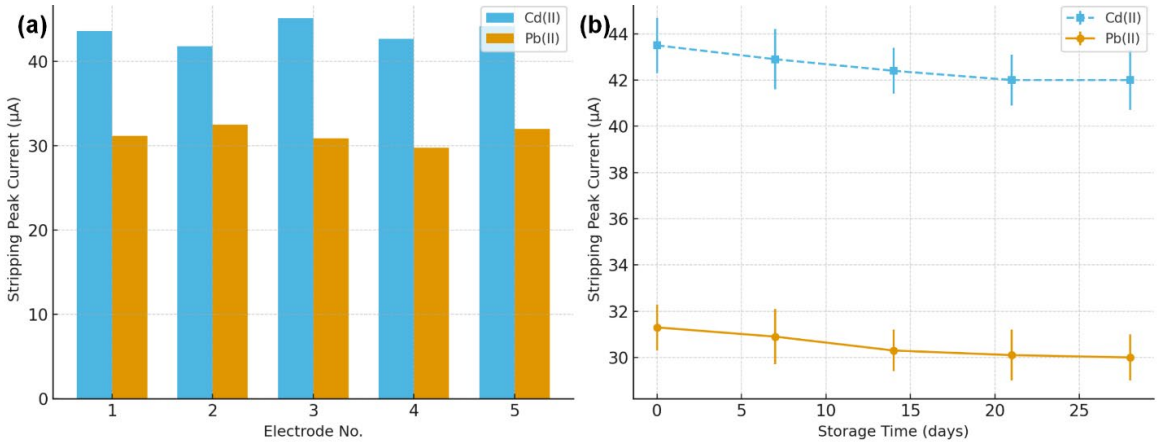

Figure 11: (**a**) $AgBiS_2$/SPE's reproducibility for the simultaneous detection of Cd(II) and Pb(II) with low RSD values; (**b**) the sensor's long-term stability test over a 28-day period, which retained over 95% of the original response.

The concentrations of Pb(II) and Cd(II) in actual environmental samples, namely tap and river water, were measured in order to confirm the proposed sensor's practical application. The conventional addition procedure was used to evaluate the samples after they had been filtered. The initial Both samples' levels of Pb(II) and Cd(II) were under the sensor's detection limit, according to the data, which are compiled in Table 2. The sensor produced readings with low RSDs (≤4.5%) and outstanding recovery rates, ranging from 97.5% to 104.2%, after spiking the samples with known concentrations of the metal ions. ICP-MS analysis was performed on the same spiked samples to confirm the electrochemical method's accuracy. The accuracy and dependability of the suggested sensor for practical uses were confirmed by the $AgBiS_2$/SPE findings, which showed excellent agreement with the ICP-MS analysis results.

Table 2: Determination of Pb(II) and Cd(II) in spiked real water samples using the $AgBiS_2$/SPE sensor and validation with ICP-MS (n = 3).

Sample	Analyte	Spiked (µg/L)	Found by Ag-BiS_2/SPE (µg/L)	Recovery (%)	RSD (%)	Found by ICP-MS (µg/L)
Tap Water	Cd(II)	10.0	9.75 ± 0.41	97.5	4.2	9.88 ± 0.35
		50.0	51.2 ± 2.30	102.4	4.5	50.6 ± 2.12
	Pb(II)	10.0	10.42 ± 0.45	104.2	4.3	10.21 ± 0.40
		50.0	49.6 ± 2.08	99.2	4.2	50.9 ± 1.98
River Water	Cd(II)	10.0	10.15 ± 0.39	101.5	3.8	10.33 ± 0.41
		50.0	52.0 ± 2.13	104.0	4.1	51.5 ± 2.05
	Pb(II)	10.0	9.89 ± 0.43	98.9	4.3	10.05 ± 0.38
		50.0	50.8 ± 2.23	101.6	4.4	51.2 ± 2.10

4 Conclusion

This work concludes by providing a clear example of how to develop and use a novel galvanic sensor that uses bismuth silver sulfide nanomaterials for the simultaneous identification of both cadmium and lead. To create high-purity, crystalline, quasi-spherical $AgBiS_2$ nanoparticles with an average diameter of around 20 nm, a simple, affordable, and environmentally benign hydrothermal technique supported by biomolecules was used. created. The intended structural, compositional, optical, and surface characteristics of the nanomaterial were validated by a comprehensive suite of characterization methods, including XRD, TEM, XPS, FTIR, UV-vis, and BET. These $AgBiS_2$ nanoparticles were added to a disposable screen-printed electrode using a simple drop-casting technique. A threefold decrease in charge transfer resistance as compared to the bare electrode demonstrated the resultant $AgBiS_2$/SPE sensor's markedly increased electrochemical activity. The sensor showed exceptional analytical performance for the simultaneous determination of Pb(II) and Cd(II) under optimal SWASV conditions. In addition to having broad linear ranges, good selectivity against common interfering ions, good reproducibility (RSD < 4.5%), and robust long-term stability—retaining more than 95% of its initial signal after four weeks—it provided low detection limits of 0.21 µg/L and 0.15 µg/L for Pb(II) and Cd(II), respectively. By analyzing actual water samples that had been spiked, the sensor's practical usefulness was successfully confirmed. The findings showed good correlation with the conventional ICP-MS technique and high recovery rates. The $AgBiS_2$ nanoparticles' synergistic effect, which combines the strong electrical conductivity of silver with the exceptional alloying capabilities of bismuth for lead and cadmium, is responsible for the sensor's remarkable performance. The proposed $AgBiS_2$/SPE sensor is a very promising and useful instrument for the quick, Because of its high sensitivity, superior selectivity, low cost, and ease of production using non-toxic materials, on-site monitoring of hazardous heavy metals is used in environmental and water quality applications.

Acknowledgement: Not applicable.

Funding Statement: The authors received no specific funding for this study.

Author Contributions: W.Z. was responsible for the conceptualization, project administration, and supervision of the study. W.Z. and C.L. developed the methodology and performed the investigation and formal analysis. C.L. was responsible for data curation and visualization. W.Z. prepared the original draft, and both authors contributed to the writing—review and editing. All authors have read and agreed to the published version of the manuscript.

Availability of Data and Materials: Data available on request from the authors.

Ethics Approval: Not applicable.

Conflicts of Interest: The authors declare no conflicts of interest to report regarding the present study.

References

1. Bouida L, Rafatullah M, Kerrouche A, Qutob M, Alosaimi AM, Alorfi HS, et al. A review on cadmium and lead contamination: sources, fate, mechanism, health effects and remediation methods. Water. 2022;14(21):3432. https://doi.org/10.3390/w14213432.

2. Ebrahimi M, Khalili N, Razi S, Keshavarz-Fathi M, Khalili N, Rezaei N. Effects of lead and cadmium on the immune system and cancer progression. J Environ Health Sci Engineer. 2020;18(1):335–43. https://doi.org/10.1007/s40201-020-00455-2.
3. Zarcinas BA, Ishak CF, McLaughlin MJ, Cozens G. Heavy metals in soils and crops in Southeast Asia. Environ Geochem Health. 2004;26(3–4):343–57. https://doi.org/10.1007/s10653-005-4669-0.
4. Verma P, Kalra N, Verma S. Advancement in sensory identification of heavy metal contamination in water: a review on progression from spectroscopic analytical techniques to handheld sensors. Microchem J. 2024;205:111293. https://doi.org/10.1016/j.microc.2024.111293.
5. Tian Y, Liu J, Qiao J, Ge F, Yang Y, Zhang Q. Advancements in electrochemical sensing technology for heavy metal ions detection. Food Chem X. 2025;25:102204. https://doi.org/10.1016/j.fochx.2025.102204.
6. Pratiwi NH, Azis MY, Setyorini DA, Rahayu RS. Anodic stripping voltammetry for simultaneous determination of lead and cadmium using bismuth-based electrodes. Anal Bioanal Electrochem. 2022;14:331–47.
7. Zhao Z. Nanomaterials-based electrochemical sensors for heavy metal ions detection. Trans Mater Biotechnol Life Sci. 2024;4:51–5. https://doi.org/10.62051/dryvdg59.
8. Zhao M-M, Wu H-Z, Deng X-K, Yi R-N, Yang Y. The application progress of magnetic solid-phase extraction for heavy metal analysis in food: a mini review. Anal Methods. 2024;16:333–43. https://doi.org/10.1039/D3AY01617J.
9. Gopi PK, Sanjayan CG, Akhil S, Hunsur Ravikumar C, Thitamadee S, Kongpatanakul S, et al. Silver bismuth sulphide ($AgBiS_2$)-MXene composite as high-performance electrochemical sensing platform for sensitive detection of pollutant 4-nitrophenol. Electrochim Acta. 2024;498:144616. https://doi.org/10.1016/j.electacta.2024.144616.
10. Alagumalai K, Sivakumar M, Kim SC, Babulal SM, Ouladsmane M. $AgBiS_2$ embedded activated graphene nanolayer for sensing azathioprine in biospecimens. Colloids Surf A Physicochem Eng Aspects. 2024;685:133243. https://doi.org/10.1016/j.colsurfa.2024.133243.
11. Hiba CP, Arya K, Singh B, Lakhiwal P, Mahajan CM, Mahapatra SK. Structural, optical, and electrical properties of tri-phase (AgBiS2, Bi_2S_3, and Ag_2S) formation during a hydrothermal synthesis of silver bismuth sulfide. J Mater Sci: Mater Electron. 2025;36(26):1694. https://doi.org/10.1007/s10854-025-15683-1.
12. Torres-Rivero K, Florido A, Bastos-Arrieta J. Recent trends in the improvement of the electrochemical response of screen-printed electrodes by their modification with shaped metal nanoparticles. Sensors. 2021;21(8):2596. https://doi.org/10.3390/s21082596.
13. Chauhan R, Fogel R, Purcarea C, Necula-Petrareanu G, Fanjul-Bolado P, Ibañez D, et al. Electrochemical characterization of carbon black in different redox probes and their application in electrochemical sensing. Carbon Trends. 2024;17:100408. https://doi.org/10.1016/j.cartre.2024.100408.
14. Magar HS, Hassan RYA, Mulchandani A. Electrochemical impedance spectroscopy (EIS): principles, construction, and biosensing applications. Sensors. 2021;21(19):6578. https://doi.org/10.3390/s21196578.
15. Kaowphong S. Biomolecule-assisted hydrothermal synthesis of silver bismuth sulfide with nanostructures. J Solid State Chem. 2012;189:108–11. https://doi.org/10.1016/j.jssc.2011.12.010.
16. Sayed R, Elmasri MM, Dhmees AS. A comparative study of particle size measurement of silver, gold and silica sand nanoparticles with different nanometrological techniques. Egypt J Chem. 2023;66:385–93.
17. Huang P-C, Yang W-C, Lee M-W. $AgBiS_2$ semiconductor-sensitized solar cells. J Phys Chem C. 2013;117:18308–14. https://doi.org/10.1021/jp4046337.
18. Mak CH, Qian J, Rogée L, Lai WK, Lau SP. Facile synthesis of $AgBiS_2$ nanocrystals for high responsivity infrared detectors. RSC Adv. 2018;8:39203–7. https://doi.org/10.1039/C8RA08509A.
19. Liang N, Chen W, Dai F, Wu X, Zhang W, Li Z, et al. Homogenously hexagonal prismatic $AgBiS_2$ nanocrystals: controlled synthesis and application in quantum dot-sensitized solar cells. Cryst Eng Comm. 2015;17:1902–5. https://doi.org/10.1039/C4CE02405B.
20. Sugarthi S, Bakiyaraj G, Abinaya R, Navaneethan M, Archana J, Shimomura M. Effect of different growth temperature on the formation of ternary metal chalcogenides $AgBiS_2$. Mater Sci Semicond Process. 2020;107:104781. https://doi.org/10.1016/j.mssp.2019.104781.
21. Senina A, Prudnikau A, Wrzesińska-Lashkova A, Vaynzof Y, Paulus F. Cation exchange synthesis of $AgBiS_2$ quantum dots for highly efficient solar cells. Nanoscale. 2024;16(19):9325–34. https://doi.org/10.1039/d3nr06128k.
22. Macchi S, Nemer M, Mills MM, Meyerson ML, Papenguth HW, Taphouse JH, et al. Comparing methods for pyrite surface area measurement through optical, aqueous, and gaseous approaches. Sci. 2025;7(1):8. https://doi.org/10.3390/sci7010008.
23. Ravele MP, Oyewo OA, Ramaila S, Mavuru L, Onwudiwe DC. Photocatalytic degradation of tetracycline in aqueous solution using copper sulfide nanoparticles. Catalysts. 2021;11(10):1238. https://doi.org/10.3390/catal11101238.

24. Bellal B, Berger MH, Trari M. Physical and photoelectrochemical properties of spherical nanoparticles of α-$AgBiS_2$. J Solid State Chem. 2017;254:178–83. https://doi.org/10.1016/j.jssc.2017.07.023.
25. Jesu Amalraj AJ, Umesh NM, Wang SF. Synthesis of core-shell-like structure SnS_2-SnO_2 integrated with graphene nanosheets for the electrochemical detection of furazolidone drug in furoxone tablet. J Mol Liq. 2020;313:113554. https://doi.org/10.1016/j.molliq.2020.113554.
26. Cheraghi S, Dasar MA, Taher MA. Fe_3O_4/RGO-ionic liquid nanocatalyst as amplifier for fabrication of highly sensitive electrochemical sensor in monitoring of thallium environmental fluids. J Nanostruct Chem. 2025;15:152510.
27. Wu Y, Gao X, Li Y. Electrochemical sensors based on polyaniline nanocomposites for detecting Cd(II) in wastewater. Int J Electrochem Sci. 2024;19(3):100519. https://doi.org/10.1016/j.ijoes.2024.100519.
28. Jia L, Lei Z, Zare N, Wu T, Ghalkhani M, Wan L, et al. Ti_3C_2 MXene-enhanced electrochemical biosensors for prostate-specific antigen (PSA) detection in prostate cancer. J Nanostruct Chem. 2025;15:152502. https://doi.org/10.57647/jnsc.2025.1501.02.